Applied Surface Science 497 (2019) 143748

Contents lists available at ScienceDirect

Applied Surface Science

journal homepage: www.elsevier.com/locate/apsusc

Full length article

Multifunction applications of $Bi_2O_3:Eu^{3+}$ nanophosphor for red light emission and photocatalytic activity

J. Divya[a,b], N.J. Shivaramu[a], W. Purcell[b], W.D. Roos[a], H.C. Swart[a,*]

[a] Department of Physics, University of the Free State, Bloemfontein, ZA-9300, South Africa
[b] Department of Chemistry, University of the Free State, Bloemfontein ZA-9300, South Africa

ARTICLE INFO

Keywords:
α-$Bi_2O_3:Eu^{3+}$
XPS
Photoluminescence
Photocatalytic activity

ABSTRACT

Undoped and Eu^{3+} doped Bi_2O_3 nanophosphors were synthesized by a citrate sol-gel method. Polyethylene glycol (PEG) was used as a surfactant to control the particle sizes. The obtained nanoparticles were characterized by powder X-ray diffraction (PXRD), field emission scanning electron microscopy, X-ray photoelectron spectroscopy (XPS), diffuse reflectance, photoluminescence (PL) and photocatalytic activities. The crystal structure and purity of the synthesized samples were investigated by PXRD and it exhibited the monoclinic (α) single phase of Bi_2O_3. The high content Eu^{3+} (1.5 and 2 mol%) doped samples consisted of a mixed phase of monoclinic (α) and tetragonal (β) Bi_2O_3. The crystallite size was determined by the Scherrer equation and it was found to be in the range of 50–97 nm. The particles were irregular, agglomerated and of spherical nature and the PEG covered the surface of the undoped and $Bi_2O_3:Eu^{3+}$ particles. XPS indicated that the Bi 4f spectrum contained a doublet, which is assigned to the Bi^{3+} oxidation state. The reflectance study confirmed the decrease in the bandgap for the doped samples. PL emission, with an intense red peak at 612 nm and other peaks at 581, 592, 652 and 707 nm was observed under different excitations of 466, 528 and 534 nm. These characteristic emissions were assigned to the luminescence of Eu^{3+} centers due to the $^5D_0 \rightarrow {}^7F_J$ (J = 0, 1, 2, 3, 4) transitions, respectively. The photocatalytic activities of the undoped and $Bi_2O_3:Eu^{3+}$ nanomaterials were evaluated for the degradation of Rhodamine B (RhB) under UV–Vis irradiation. The results showed that $Bi_2O_3:Eu^{3+}$ (0.6 mol%) had a better photocatalytic activity compared to the undoped sample.

1. Introduction

In recent years, numerous studies were carried out on bismuth-based semiconductors as Bi_2O_3 is extensively used in solid state lasers, bio-imaging, temperature sensors, high refractive index, gas sensors, optical coatings, glass manufacturing and photoluminescence (PL) [1,2]. Bi_2O_3 is non-toxic, easy and cheap to prepare and is well-known as a p-type semiconductor with the wide band energy gap that can be varied between 2 and 3.9 eV [1]. As semiconductor Bi_2O_3 also has the potential to be used in the photocatalytic degradation of organic pollutants, which may reduce environmental problems such as waste water purification and air purification [3]. As reported in literature, nanocomposite photocatalysts such as $BiVO_4/WO_3$ [4], $NaBiO_3/ZnO$ [5], $MnWO_4/BiOI$ [6], In_2S_3/CuS [7] and TiO_2 thin films [8] were used to demonstrate their improved organic pollutant removal activities. Research also indicated that Bi_2O_3 is a very effective photocatalyst due to its superior oxidizing capability that can oxidize water through the direct generation of O_2^- and OH· radicals. Lately Bi_2O_3 also gained significant attention due to the high surface area of its nanomaterials, which creates a large number of adsorption sites as well as its ability to strongly absorb UV–Vis radiation [9,10].

Bi_2O_3 exists generally in five different polymorphs denoted as monoclinic (α-Bi_2O_3), tetragonal (β-Bi_2O_3), body centered cubic (γ-Bi_2O_3), face centered cubic (δ-Bi_2O_3) and orthorhombic (ε-Bi_2O_3). Among these polymorphs, the α-Bi_2O_3 phase is stable at room temperature [11]. Research results reported that the bismuth-based ions (Bi^{2+}, Bi^{3+}) are luminescent activators, which can also act as sensitizers in various host materials [12]. The emission spectra of bismuth ions appear over a large range of wavelengths, especially in the visible wavelength region [9]. A possible way to improve the luminescence efficiency of Bi_2O_3, is to dope the compound with different rare earth elements due to the similarity of the ionic radii of rare earth ions that are similar to that of Bi^{3+}.

Dutta et al. [9], reported on the PL of β-$Bi_2O_3:Eu^{3+}$ (2 mol%) nanoparticles that exhibited a broad excitation band from 250 to 400 nm and a strong peak at 322 nm, which were attributed to the charge

* Corresponding author.
E-mail address: swarthc@ufs.ac.za (H.C. Swart).

https://doi.org/10.1016/j.apsusc.2019.143748
Received 11 June 2019; Received in revised form 7 August 2019; Accepted 20 August 2019
Available online 27 August 2019

transfer band of Eu^{3+}–O^{2-} and to the excitation of Bi^{3+} ions, respectively. In addition, weak peaks at 362, 374 and a sharp peak at 395 nm were attributed to the f-f transitions of Eu^{3+} when excited at 322, 362 and 374 nm. A strong emission peak at 611 nm was attributed to the electric dipole transitions of Eu^{3+} [9]. Ashwini et al. [13] co-doped the β-phase of Bi_2O_3:Eu^{3+} with Li^+ using the sonochemical method. A series of emission peaks was observed at 580, 593, 614, 615 and 703 nm and was assigned to the Eu^{3+} transitions. The maximum PL intensity was observed for the 5 mol% Bi_2O_3:Eu^{3+} [13]. One benefit from Bi_2O_3:Eu^{3+} nanoparticles, compared to Bi_2O_3 is their higher optical absorption ability in the visible light region [9].

The current work is based on the synthesis of undoped Bi_2O_3 and Bi_2O_3:Eu^{3+} (0.1–2 mol%) nanophosphors using the citrate gel method. The effects of Eu^{3+} doping on the crystal structure, surface morphology, optical bandgap, luminescence and photocatalytic activity has been studied via the degradation of rhodamine B (RhB) in an aqueous solution under UV–Vis radiation. Results obtained from this study indicated that Bi_2O_3:Eu^{3+} nanoparticles were effective in the photocatalytic oxidation of a RhB dye solution using UV–visible irradiation.

2. Materials and methods

Bismuth nitrate pentahydrate [$Bi(NO_3)_3.5H_2O$], citric acid ($C_6H_8O_7$), polyethylene glycol [PEG400], europium nitrate pentahydrate [$Eu(NO_3)_3.5H_2O$] and Rhodamine B (RhB) were purchased from Sigma –Aldrich and used without further purification.

2.1. Preparation of undoped and europium doped bismuth oxide

The bismuth solution was prepared by dissolving 4.851 g of bismuth nitrate pentahydrate in 15 ml of nitric acid (HNO_3), the solution was stirred for 15 min at room temperature (RT), until a transparent clear solution was obtained. After that, 1.921 g of citric acid (acts as a chelating agent) was added to the mixture, which was stirred for another 15 min [14] and then 70 μL polyethylene glycol was added to this mixture (to control the nanoparticles sizes). The mixture was heated to 80 °C for 1 h to remove the excess nitrate (NO_2) in the solution and to evaporate the water. The heating was continued at 80 °C until a clear gel was obtained, which was subsequently dried overnight at 120 °C in an oven. The resultant product was ground in a mortar to obtain a fine white colour Bi_2O_3 powder and then calcinated at 600 °C for 2 h in air at a heating rate of 10 °C/min and a yellow colour product was formed. The Bi_2O_3:Eu^{3+} (0.1–2 mol%) were synthesized by following the same procedure as described above.

2.2. Characterization

Thermal stability changes were studied thermogravimetrically under a nitrogen atmosphereat a heating rate of 10 °C min^{-1}using a Mettler-Toledo TGA/SDTA851e. The structural properties of the Bi_2O_3:Eu^{3+} nanophosphors were analyzed using a Bruker D8 Advance powder x-ray diffractometer (PXRD) with a Cu Kα radiation of wavelength 0.154 nm. Scanning electron microscopy (SEM) images of the final products were obtained using a JEOL JSM-7800F microscope to perform morphology analysis. The diffuse reflectance (DR) spectra measurements were recorded using a Perkin Elmer Lambda 950 UV–VIS spectrophotometer with integrating sphere. X-ray photoelectron spectroscopy (XPS) was used to study the chemical state of the undoped and Eu doped Bi_2O_3 samples after the thermal treatment at 600 °C. The XPS analyses were carried out with a PHI 5400 XPS spectrometer using a non-monochromatic Mg Kα X-ray source (1253.6 eV, 15 kV, 300 W) and hemispherical sector analyzer. The photoelectron take-off angle for all measurements was 45°. Survey scans were done with a pass energy of 178.95 eV in energy steps of 0.25 eV and dwell time of 100 ms. High resolution scans used a pass energy of 44.75 eV and step size 0.125 eV. Charge correction was done by correcting to the C—C bond at a binding energy of 284.7 eV. The XPS high resolution spectra were analyzed using XPS PEAK 4.1 software. A Cary Eclipse spectrophotometer with a monochromatized xenon flash lamp as the excitation source, was used at room temperature (RT – 23 °C) for the PL measurements of the isolated phosphor products.

The photocatalytic activity of the undoped and Bi_2O_3:Eu^{3+} was investigated at RT by determining their influence in the extent and rate of RhB degradation. A hallow cylindrical immersion type photocatalytic reactor equipped with a glass water jacket was used for the degradation study. The photocatalytic experiments were performed under irradiation of a 250 W UV–visible lamp. The lamp was placed in the inner part of the photocatalytic reactor and cooling water was circulated through the water jacket surrounding the lamp keeping the setup at RT. The initial concentration of the RhB was 0.01 mmol/L. 0.4 g of the photocatalyst was added into 50 ml of the RhB solution. Prior to the photocatalytic experiments, the suspensions were stirred for approximately 3 h in the dark at room temperature to ensure the establishment of an adsorption-desorption equilibrium between the catalyst and RhB molecules and then the suspension was exposed to UV–visible light irradiation using the UV–visible lamp. The glass reactor was mounted on a magnetic stirrer to keep the suspension homogeneous during irradiation. A 5 ml aliquot of the suspension solution was collected after every 15 min (until decolonization of the dye solution) of UV–Visible light irradiation, with a maximum irradiation of 120 min. These aliquots were centrifuged to remove the catalyst particles. The RhB concentrations were monitored as a function of absorbance change in the 400–700 nm range using an UV–Vis spectrometer.

3. Results and discussion

3.1. TGA analysis

Fig. 1 shows the TGA analytic results of the as-synthesized sol-gel Bi_2O_3 and Bi_2O_3:Eu^{3+} (1 mol%) powders. The measuring temperature ranged from 40 to 700°C with a heating rate of 10 °C/min. Fig. 1 indicates four major drops, for the first region (i) the weight loss occurred between 47.8 and 153.2 °C(1.92%) and 49.1–148 °C (2.29%) for undoped and Bi_2O_3:Eu^{3+} samples and was due to the evaporation of water and moisture from the powder [15]. The region (ii) decomposition step in the range 152.8–226.7 °C (4.99%) and 148.4–228 °C (7.70%) was attributed to the loss of water molecules from $Bi(NO_3)_3.5H_2O$ and $Eu(NO_3)_2.5H_2O$ in which dehydrated oxide was formed [15,16]. In region (iii) the weight loss appeared in the range of 226.7–381.5 °C (31.24%) and 228–364.6 °C (29.44%), the weight loss was observed due to the decomposition of Bi/Eu –citrate to produce $Bi_2(Eu)O_3$ with the burnout/decomposition of the citric anions and PEG as CO_2 and H_2O. A small weight loss was further observed (region (iv)) in between 400 and 546 °C for undoped (1.11%) and doped (0.90%) samples due to the decomposition of the remaining citric acid and PEG. Similar results

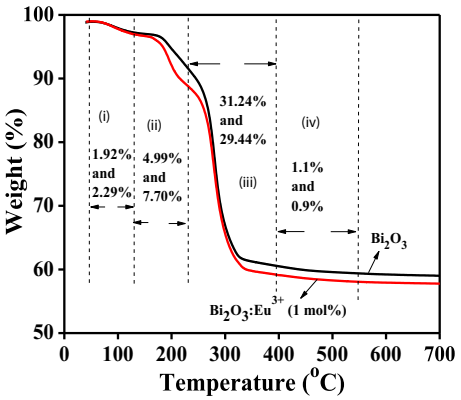

Fig. 1. TGA spectrum of Bi_2O_3 and Bi_2O_3:Eu^{3+} (1 mol%).

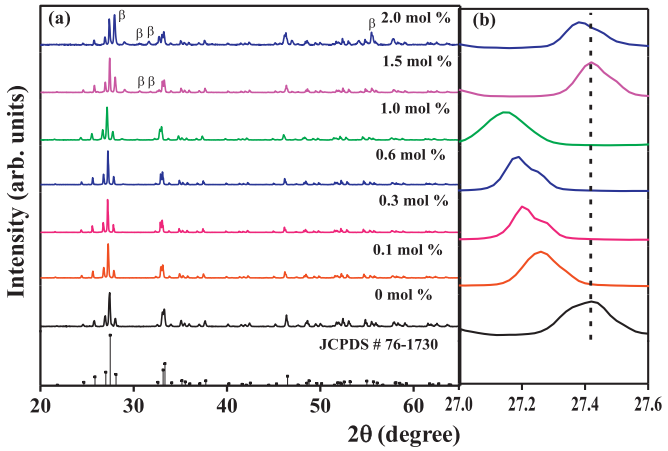

Fig. 2. (a) XRD patterns of Eu^{3+} (0–2 mol%) doped Bi_2O_3 and (b) diffraction peak corresponding to the (120) crystallographic plane of Eu^{3+} (0–2 mol%) doped Bi_2O_3.

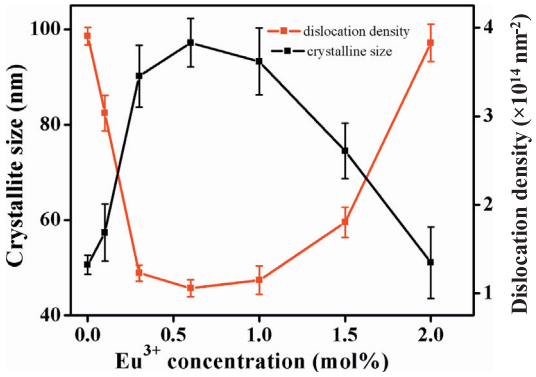

Fig. 3. Variation graph of crystallite size and dislocation density as a function of Eu^{3+} content in Bi_2O_3.

were obtained by other researchers. May-Show Chen et al., [17] reported TGA analysis for sol-gel synthesized Bi_2O_3 material and their measuring temperature ranged between 50 and 800 °C, with a heating rate of 10 °C/min. The TGA curve contains three steps: (i) 50–120 °C, evaporation of physical-adsorbed water on bismuth oxide powders, resulting in about 1.3% weight loss; (ii) 120–350 °C, thermal decomposition and burnout of glacial acetic acid and 2-methoxyethanol, resulting in 24.8% weight loss; and (iii) between 600 and 800 °C, a steady state was obtained. The total weight loss was 30.9% after a 50–800 °C heat treatment. In the present work, a steady state was observed for the temperature range of 550–700 °C and the total weight loss was 39.26% and 40.33% for undoped and doped samples.

3.2. X-ray diffraction

The crystal structure of the undoped and Bi_2O_3:Eu^{3+} doped products were investigated by PXRD. Fig. 2(a) shows that all the diffraction peaks of undoped and (0.1–1 mol%) Bi_2O_3:Eu^{3+} matched well with the monoclinic structure of Bi_2O_3 with space group $P_{2i/c}$ after calcinated at 600 °C (JCPDS # 76-1730) [18]. At higher content (1.5 and 2 mol%) of Eu^{3+} the 2θ peaks consisted of a mixed α/β phase of Bi_2O_3. No Eu^{3+} or any other impurity phases could be detected. The 2θ peaks at 27.9°, 30.5°, 31.6° and 55.5° correspond to the (221), (311), (002) and (621) planes of the tetragonal structure of Bi_2O_3 (JCPDS # 74-1374) [19] with space group $C\bar{4}b2$. In addition, we observed that the diffraction peak of the (120) plane systematically shifts towards the low angle side of the 2θ position with increasing Eu^{3+} content upto 1 mol%. It is an indication that the Eu^{3+} ions were replacing some of the Bi^{3+} sites in the six co-ordinated α-Bi_2O_3 [20]. The ionic radius of Eu^{3+} (0.95 Å) is slightly smaller than the Bi^{3+} (1.03 Å), resulting in a shrinkage of the crystal unit cell volume. On the other hand, a further, increase of the Eu^{3+} content results in a shift towards the higher angle side position (Fig. 2(b)). A possible explanation is that at the higher Eu^{3+}content studies, the Eu^{3+} ions occupies the interstitial sites or grain boundaries, which resulted in the formation of the α/β mixed phase.

The calculated lattice constants (a, b and c), interstitial angles (α, β and γ) and unit cell volumes (Program Unit Cell software (T.J.B. Holland, S.A.T. Redfern, Department of Earth Science, Cambridge, U.K, 1995) are tabulated in Table 1. The calculated values compares well with those reported in the standard file (JCPDS #76-1730). The crystallite sizes were calculated using the Debye Scherrer formula and the values are reported in Table 1. The crystallite sizes steadily increased upto the 0.6 mol% Eu^{3+} doped sample, then decreased with a further increase of the Eu^{3+} content. Simultaneously the dislocation density and lattice strain decreased with an increase in Eu^{3+} content upto 0.6 mol%, which mirrors (inversely relationship) the crystallite size

Table 1
Crystal structure parameters of Bi_2O_3:Eu^{3+} (0–2 mol%) nanophosphor.

Content of Eu^{3+} (mol%)	Crystallite size (nm)	Strain (%)	Dislocation Density × 10^{14} (nm^{-2})	Lattice constants (Å)	β (degree) (α = γ = 90°)	Cell volume ($Å^3$)
0	50.6 ± 2	0.070	3.906	a = 5.838 b = 8.146 c = 7.486	66.96	327.64
0.1	57.4 ± 6	0.065	3.035	a = 5.860 b = 8.181 c = 7.513	67.321	332.45
0.3	90.2 ± 6.5	0.040	1.229	a = 5.854 b = 8.193 c = 7.536	67.172	333.18
0.6	97.2 ± 5.1	0.039	1.058	a = 5.851 b = 8.188 c = 7.530	67.160	332.49
1	93.3 ± 7	0.041	1.149	a = 5.831 b = 8.194 c = 7.534	67.340	332.88
1.5	74.5 ± 5.8	0.049	1.802	a = 5.848 b = 8.164 c = 7.507	66.780	329.78
2	51.1 ± 7.5	0.075	3.830	a = 5.806 b = 8.171 c = 7.509	67.660	328.88

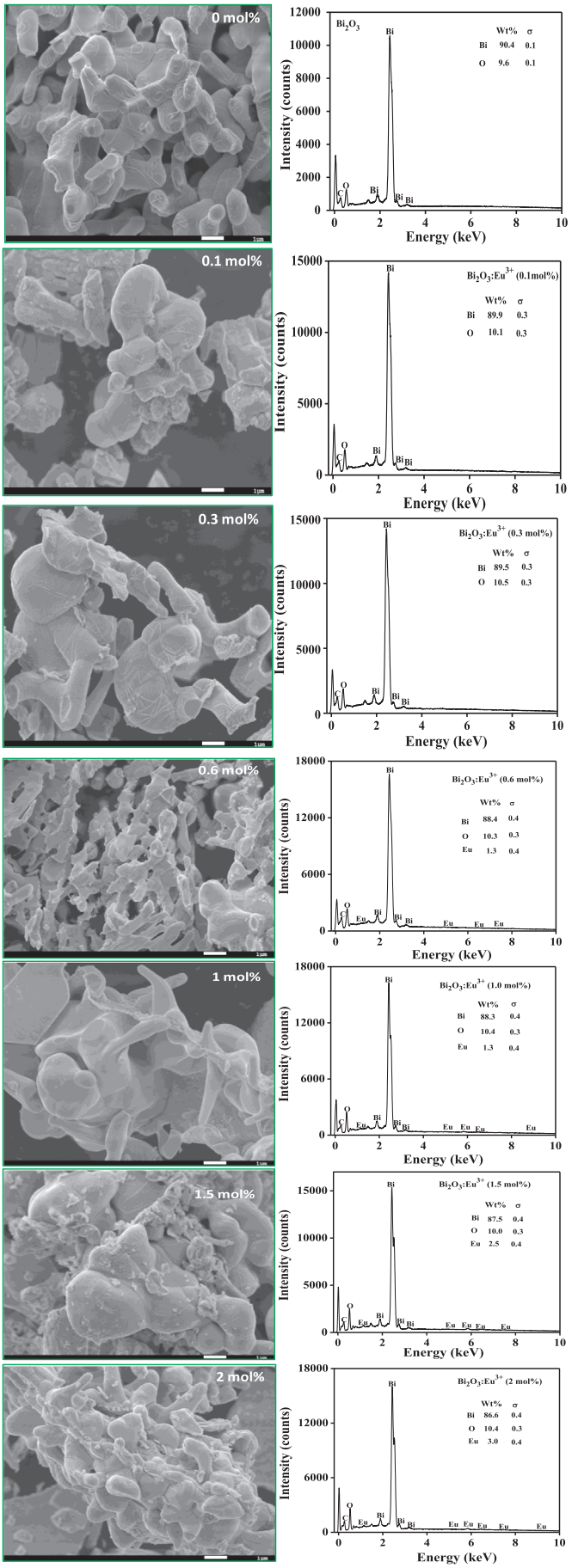

Fig. 4. SEM imagesand EDAX of Eu^{3+} doped (0–2 mol%) Bi_2O_3 nanophosphors.

increase as shown in Fig. 3. This decrease in dislocation density indicates that the dopant ions were dissolved in the Bi_2O_3 lattice. An increase in the Eu^{3+} content from 1 to 2 mol% led to a decrease in the crystallite size with an increase of dislocation density and lattice strain, which is attributed to the dopant ions, which possibly occupied sites on the grain boundaries [21,22].

3.3. Surface morphology and elemental analysis

Fig. 4 shows SEM images of the different Bi_2O_3:Eu^{3+} (0–2 mol%) products synthesized and calcinated at 600 °C. All the images indicate particles of irregular shape and of an agglomerated spherical nature with average particle size of approximately 90 nm. The layer-like stuctures of all the products in Fig. 4 confirm that the PEG successfully covered the surfaces of the undoped and Bi_2O_3:Eu^{3+} particles. The results also indicate an increase in particle agglomeration density with increasing Eu^{3+} content upto 1 mol%. The further increase in dopant content resulted in the formation of the particles irregular in shape. EDAX confirmed the presence of Bi, O and C elements in all the synthesized samples as shown in Fig. 4. The carbon content is possibly the remnants from the decomposed PEG, which initially covered the Bi_2O_3 particle surfaces and or the carbon tape used. The results also confirm that the citrate gel method is an effective process to produce Bi_2O_3 particles. The EDAX spectra for (0.1–0.2 mol%) Eu^{3+} doped samples do not show the presence of any Eu^{3+} in the final product, which is attributed to the low content of the Eu^{3+} and the EDAX inability to detect trace amounts of elements on products. Eu^{3+} was only detected at 0.2 mol% and higher content due to the relatively higher content. The wt% of the Bi is expected to decrease with an increase in the Eu^{3+} content, which is in fact observed in Fig. 4, confirming the successful substitution of Bi^{3+} by Eu^{3+} in the final products.

3.4. Diffused reflectance

The optical reflectance of Bi_2O_3 and Bi_2O_3:Eu^{3+} (0.1–2 mol%) were also investigated using diffused reflectance spectra at room temperature and are shown in Fig. 5(a). The absorption below 418 nm for the pure Bi_2O_3 product is attributed to the charge transfer from the valence band to the conduction band, which normally results in high absorption in the visible region. With the introduction of Eu^{3+} the absorption edge shifts towards higher wavelengths. This visible light response of Bi_2O_3:Eu^{3+} nanophosphors can be attributed to the formation of surface-defects such as oxygen vacancies or OH· radicals [10], which facilitate the increase in photocatalytic activity under visible light conditions. The results in Fig. 5(a) indicate that the absorption edge at 466 nm for Eu^{3+} doped samples became stronger with an increase in Eu^{3+} content and is assigned to the $^7F_0 \rightarrow {}^5D_2$ transition within Eu^{3+}. These results also correlated well with the PL results.

The bandgap values of the samples were estimated using the Kubelka-Munk function [23]:

$$F(R_\infty) = (1 - R_\infty)^2/R_\infty$$

where, $R_\infty = R_{sample}/R_{standard}$, R_{sample} is the reflectance of the sample and $R_{standard}$ is the reflectance of the $BaSO_4$ (reference) sample. The optical bandgap were obtained from the energy axis intercept of the plots of $[F(R_\infty)\, h\nu]^{1/2}$ versus the incident photon energy, E (in eV) and is shown in Fig. 5(b). The optical indirect bandgap value was estimated to be 2.75 eV for pure Bi_2O_3 and varies between 2.50 and 2.77 eV for Bi_2O_3:Eu^{3+} (0.1–2 mol%) doped samples, respectively. The direct bandgap values were estimated to be 2.88 eV for Bi_2O_3 and 2.78–2.90 eV for the Bi_2O_3:Eu^{3+} doped(0.1–2 mol%) samples as shown in Fig. 5(c) and the change in direct bandgap values are attributed to the interaction between the Eu^{3+} ions and Bi_2O_3 [9] in the final products. The reported optical bandgap values compared well with the present results [9]. Y. Shi et al., reported that the energy bandgap of α-Bi_2O_3prepared via the solvothermal–calcination method was observed

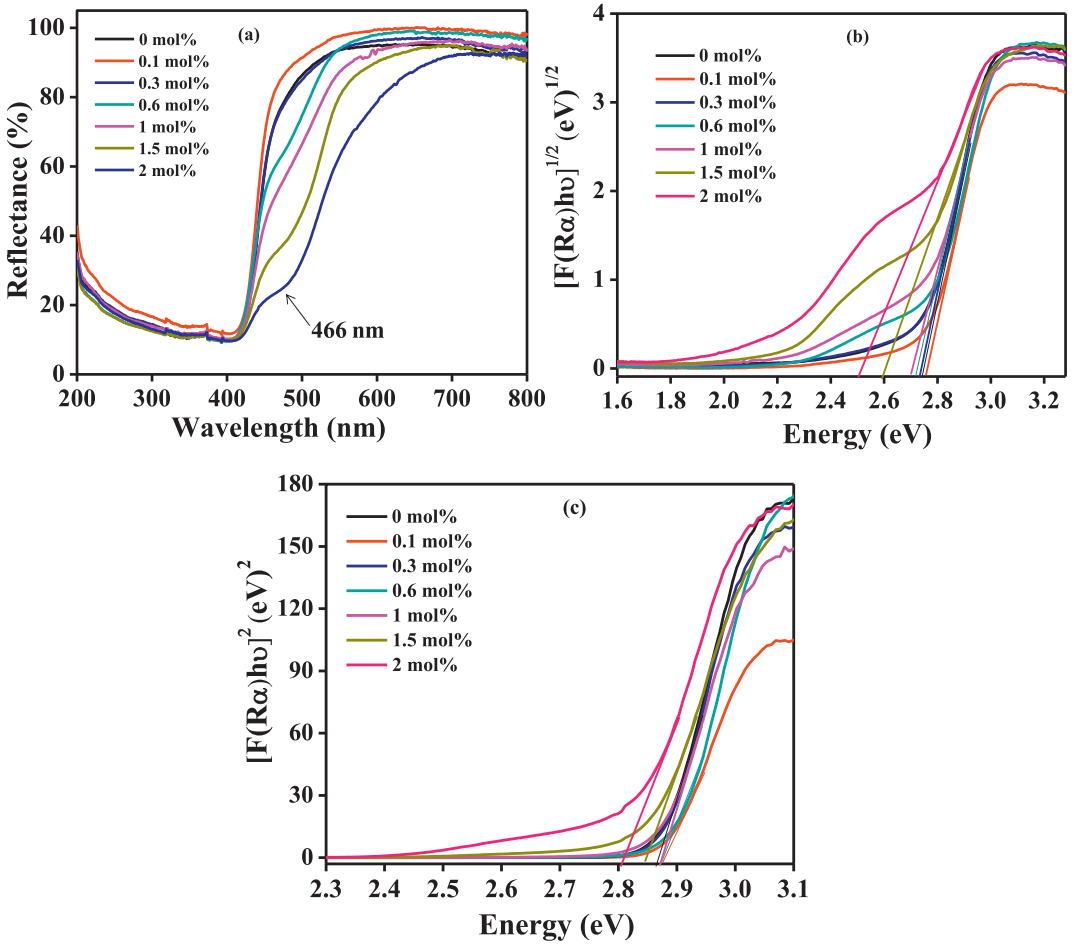

Fig. 5. (a) Diffused reflectance spectra (b) plots of $(F(R_\infty)h\vartheta)^{1/2}$ and (c) $(F(R_\infty)h\vartheta)^2$ versus photon energy of Eu^{3+} doped (0–2 mol%) Bi_2O_3.

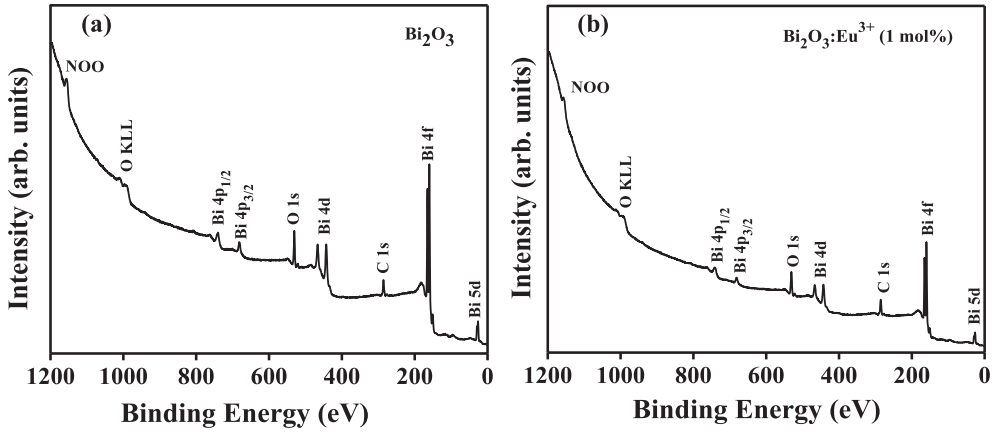

Fig. 6. XPS survey spectra: (a) undoped Bi_2O_3 and (b) Bi_2O_3:Eu^{3+} (1 mol%).

at 2.85 eV [24]. D. P. Dutta et al., [9] reported that undoped α-Bi_2O_3 nanorods exhibit a bandgap of 3.81 eV, which change to 3.79 eV in the case of the Bi_2O_3:Eu^{3+} (2%). Shuxing Wu et al., [25] reported that the bandgap values of Bi_2O_3 doped with 1% La and Ce samples are smaller compared to that of undoped Bi_2O_3, and attributes this change in bandgap to the observed increase in the visible light absorption. A possible explanation is that the newly introduced Eu^{3+} ions create "allowed" shallow states with small ionisation energies in the bandgap of the host material. An increase in Eu^{3+} content (higher density) then generates a band very close to the valence or conduction band edge resulting in the observed decrease in bandgap values [26].

3.5. X-ray photoelectron spectroscopy

The chemical analysis of the undoped and Bi_2O_3:Eu^{3+} doped (1 mol %) nanocrystals were performed with XPS. The XPS wide survey spectrum of the undoped and doped Bi_2O_3 products are shown in Fig. 6 (a) and (b). The expected Bi, O, C and O KLL peaks were detected as shown in Fig. 6 (a) and (b). The observed carbon is probably due to adsorbed atmospheric hydrocarbons or the remains of the decomposed PEG and citrate, or as a result of atmospheric exposure or during the calcination at high temperature. All binding energies were corrected for the charge shift using the C 1s peak of graphitic carbon

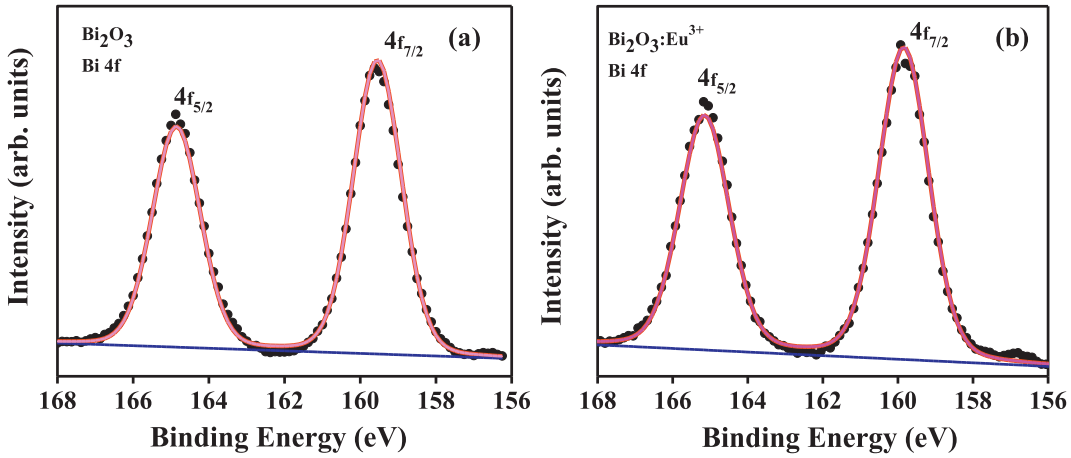

Fig. 7. Bi 4f high resolution spectra: (a) undoped Bi_2O_3 and (b) Bi_2O_3:Eu^{3+} (1 mol%).

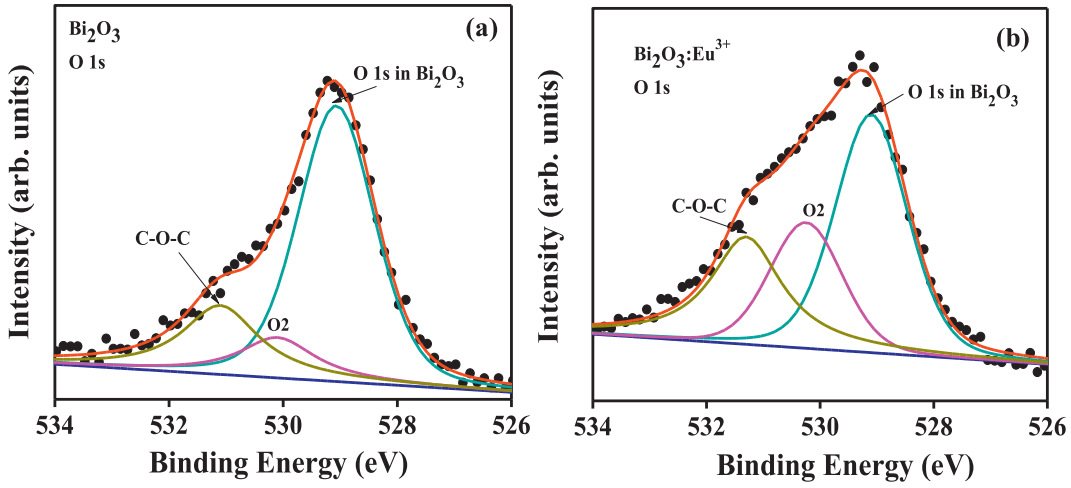

Fig. 8. O 1s high resolution spectra: (a) undoped Bi_2O_3 and (b) Bi_2O_3:Eu^{3+} (1 mol%).

Table 2
Binding energies of the deconvoluted peaks of the Bi 4f, O 1s, C 1s and Bi 4f/O 1s ratio of the Bi_2O_3 and Bi_2O_3:Eu^{3+} samples.

State		Bi_2O_3				Bi_2O_3:Eu^{3+}			
		BE (eV)	Area	β (eV)	Bi4f/O1s ratio	BE (eV)	Area	β (eV)	Bi4f/O1s ratio
Bi4f	$4f_{7/2}$	158.7	88,645.1	1.57	4.70	158.8	30,347.1	1.57	1.65
	$4f_{5/2}$	164.0	66,665.3	1.57	3.54	164.1	25,613.8	1.57	1.39
O1s	Bi_2O_3	529.1	18,851.7	1.55		539.1	18,371.2	1.55	
	O2	530.1	3617.1	1.55		530.2	9379.1	1.55	
	C-O-C	531.1	6174	1.55		531.2	10,989.6	1.55	
C1s	Carbide	283.1	4630	1.55		283.3	6206.6	1.55	
	C-C	284.7	14,438.1	1.55		284.7	12,629.2	1.55	
	C-O-C	285.7	5049.6	1.55		285.5	6792.7	1.55	

(BE = 284.7 eV), which was used as a reference. [27]. The XPS spectrum did not predict the chemical state of Eu possibly due to its low concentration or maybe due to its low atomic sensitive factor i.e. 2.488 [27].

The XPS for the Bi 4f spectrum contains a doublet with binding energies equal to 158.7and 164.0 eV for the undoped Bi_2O_3 product compared to the Bi_2O_3:Eu^{3+} doped samples, which has binding energies of 158.8 and 164.1 eV, indicating that the Bi was in the Bi^{3+} state, as shown in Fig. 7(a–b). These results compares well with previously research results with an energy difference of 5.3 eV between the $4f_{7/2}$ and $4f_{5/2}$ orbital's, which is equal [28]. Fig. 8 (a–b) show the detail energy region for the oxygen (O)1 s level for the undoped and Bi_2O_3:Eu^{3+} samples. The O 1 s fits revealed O in Bi_2O_3 while the O2 peak might be due to defects in the crystal, which can be related to oxygen (oxygen vacancy or/and oxygen interstitial) [29] or OH· radicals while the third peak is assigned to C-O-C for both undoped and Bi_2O_3:Eu^{3+} samples. The corresponding binding energies were tabulated in Table 2. The C-O-C and OH^- peaks were probably coming from atmospheric hydrocarbons such as CO_2 and H_2O groups or decomposed PEG and citrate. Fig. 9(a–b) shows the deconvoluted carbon C 1s peaks for both the samples. The components on the low binding energy side on the wide survey spectrum at 283.1, 284.7 and 285.7 eV for the Bi_2O_3 and 283.3, 284.7 and 285.5 eV for the Bi_2O_3:Eu^{3+} are attributed to carbide, C—C and C-O-C [27,28]. The full width at half maxima (β) and

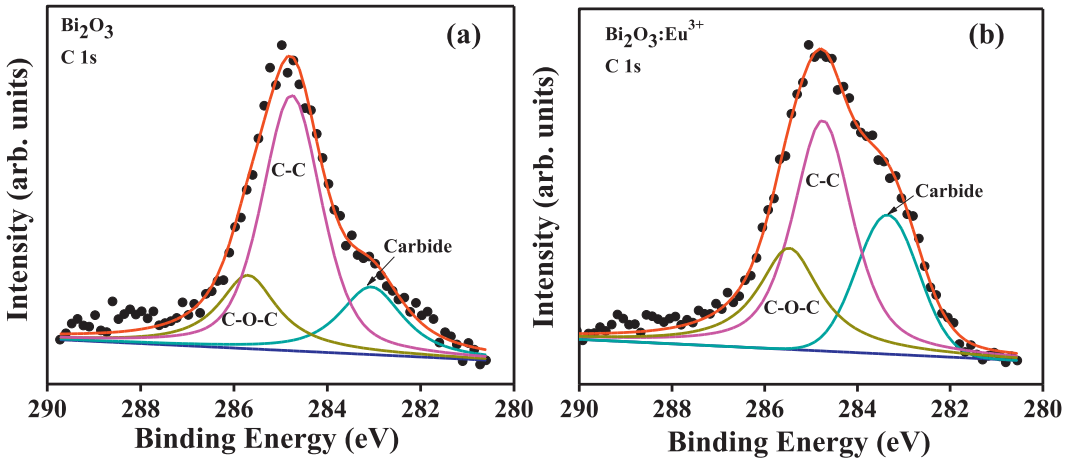

Fig. 9. C 1s high resolution spectra: (a) undoped Bi_2O_3 and (b) Bi_2O_3:Eu^{3+} (1 mol%).

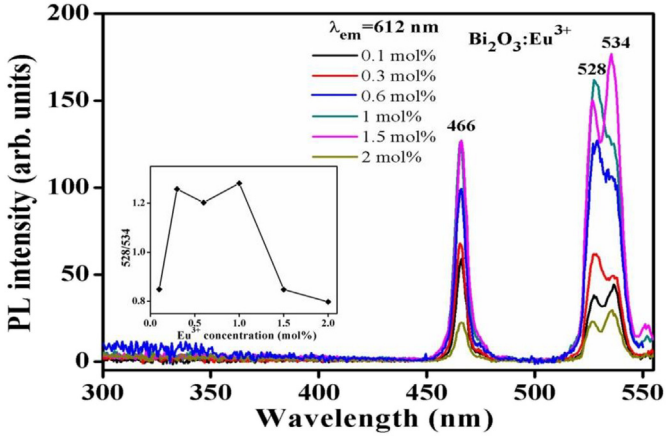

Fig. 10(a). Excitation spectra of Bi_2O_3:Eu^{3+} with different dopant content. Inset figure represents the relative intensity ratio of the 528 nm/534 nm intensities with Eu^{3+} content.

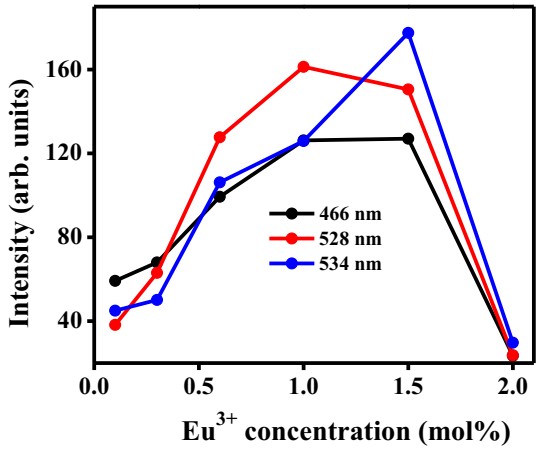

Fig. 10(b). The variation of the excitation intensity of Eu^{3+} as a function of doping content.

area of the all deconvoluted peaks for the Bi_2O_3 and Bi_2O_3:Eu^{3+} samples are tabulated in Table 2. The results confirmed that the area of the Bi $4f_{7/2}$ and Bi $4f_{5/2}$ peaks decreased with the addition of Eu^{3+} into the Bi_2O_3 lattice, while the area of the O 1 s peaks did not change noticeably. The O2 peak on the other hand increased substantially and is attributed to the small variation in ionic radius between the Bi^{3+} and

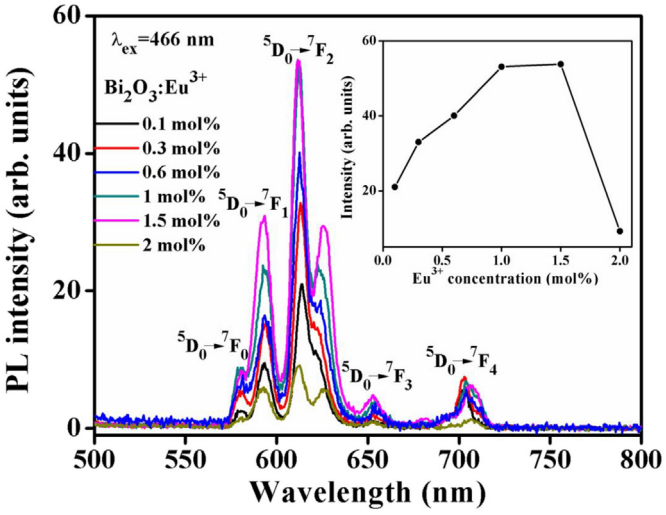

Fig. 11(a). Emission spectra of the Bi_2O_3:Eu^{3+} with different dopant content (λ_{ex} = 466 nm). Inset figure represented as PL intensity (λ_{em} = 612 nm) with Eu^{3+} content.

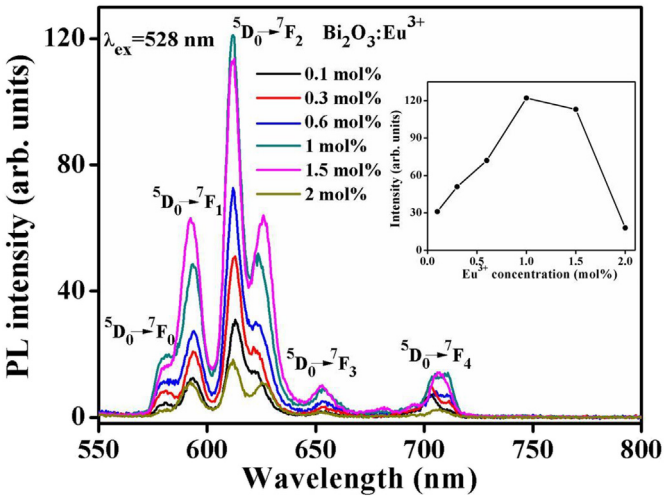

Fig. 11(b). Emission spectra of the Bi_2O_3:Eu^{3+} with different dopant content (λ_{ex} = 528 nm). Inset figure represents PL intensity (λ_{em} = 612 nm) with Eu^{3+} content.

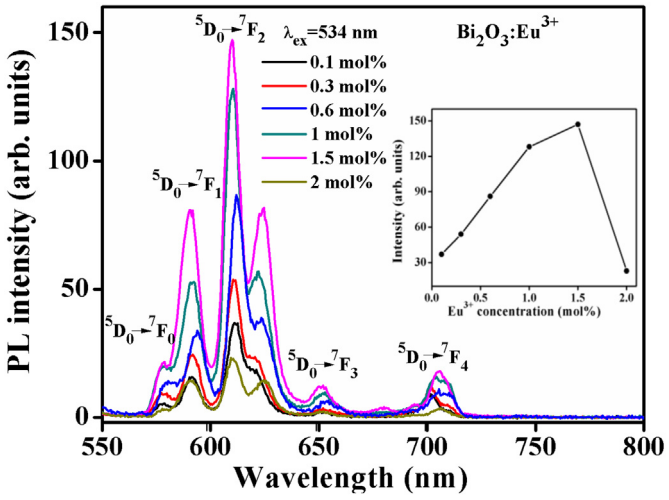

Fig. 11(c). Emission spectra of the $Bi_2O_3:Eu^{3+}$ with different dopant content (λ_{ex} = 534 nm). Inset figure represents PL intensity (λ_{em} = 612 nm) with Eu^{3+} content.

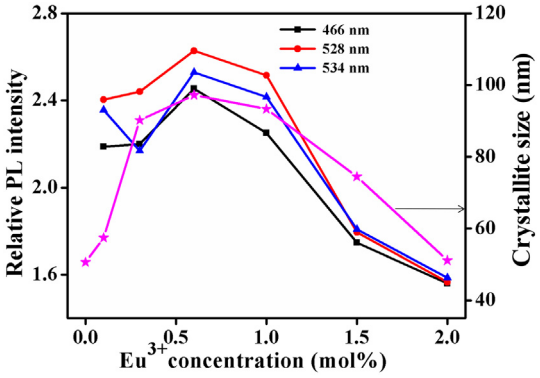

Fig. 12. The variation of the relative PL intensity and crystallite size with various Eu^{3+} content.

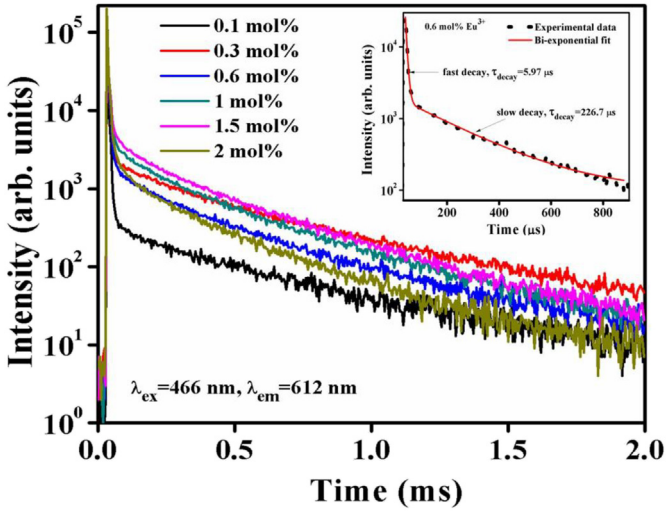

Fig. 13. PL decay curves of the $Bi_2O_3:Eu^{3+}$ with different dopant content. Inset figure represented a Bi-exponential fitted graph.

Table 3
Decay times obtained by using a 467 nm for the excitation and by monitoring the most intense line at 612 nm for $Bi_2O_3:Eu^{3+}$.

$Bi_2O_3:Eu^{3+}$ (x mol%)	A_1	A_2	τ_1 (µs)	τ_2 (µs)
0.1	22,587	295	5.57	409.2
0.3	43,839	1935	5.90	384.8
0.6	47,495	1664	5.97	226.7
1.0	44,446	2899	7.36	285.5
1.5	40,434	3617	8.19	289.5
2.0	45,903	1719	7.46	243.9

Eu^{3+} resulting in the formation of oxygen vacancies or/and oxygen interstitial. The ratios between the areas under the Bi 4f and O 1 s peaks for the undoped and $Bi_2O_3:Eu^{3+}$ samples also decreased after doping.

3.6. Photoluminescence

The excitation spectra of $Bi_2O_3:Eu^{3+}$ (0.1–2 mol%) phosphors are reported in Fig. 10(a). The excitation spectra consist of peaks at 466, 528 and 534 nm, which are due to the $^7F_0 \rightarrow ^5D_2$, $^7F_0 \rightarrow ^5D_1$ and $^7F_1 \rightarrow ^5D_1$ transitions, respectively [30]. The prominent peak at 466 nm predict that this phosphor is a promising candidate for colour converters in LEDs under a blue LED excited red phosphor. A very distinctive change in excitation peak intensities is visible for the different Eu^{3+} content. Also notable is that the increase in Eu^{3+} content in the samples resulted in an intensity increase in the excitation peaks at 528 nm upto 1 mol% Eu^{3+} content, while the 466 and 534 nm peaks increased for Eu^{3+} content up to 1.5 mol%, as shown in Fig. 10(b). These results indicate that the ratio of the $^7F_0 \rightarrow ^5D_1$ to $^7F_1 \rightarrow ^5D_1$ (528 nm/534 nm) transitions has increased with increasing Eu^{3+} content, which confirmed that the ratio value of the 528 nm/534 nm for 0.3–1 mol% Eu^{3+} is > 1, which is attributed to the strong energy transfer from the $^7F_0$ to $^5D_1$ energy level of the Eu^{3+} state as shown in the inset of Fig. 10(a).

The emission spectra of the $Bi_2O_3:Eu^{3+}$ phosphors excited at 466, 528 and 534 nm at RT are shown in Figs. 11(a)–11(c), respectively. All samples doped with Eu^{3+} ions exhibited bright red luminescence when excited with the xenon lamp as indicated in Figs. 11(a)–11(c). The spectra consist of five sets of emission peaks that are situated at ~580, 593, 612, 651 and 703 nm which are assigned to the $^5D_0 \rightarrow ^7F_J$ (J = 0, 1, 2, 3, 4) transitions in the Eu^{3+} ions, respectively [29]. Among these, the peak at 612 nm was the most dominant and is due to the presence of the electric dipole transition and which is usually very sensitive to the local crystal coordination. The transition at 593 nm ($^5D_0 \rightarrow ^7F_1$) on the other hand is insensitive to the crystal coordination because of the significant/prominent magnetic dipole transition.

The variation of the PL intensity as a function of dopant content is also evident from the results reported in the insets of Figs. 11(a)–11(c). The maximum intensity for the 1.5 mol% $Bi_2O_3:Eu^{3+}$ was observed for the 466 and 534 nm excitation wavelengths and at 528 nm excitation wavelength for the 1 mol% $Bi_2O_3:Eu^{3+}$. Thereafter, the maximum intensities decreased due to concentration quenching. The $^5D_0 \rightarrow ^7F_1$ and $^5D_0 \rightarrow ^7F_2$ transitions plays a vital role in the Eu^{3+} emission spectra due to the local environment of the Eu^{3+} in the host lattice [31]. The integral intensity ratio of the electric-dipole to magnetic-dipole transition is widely used to probe the degree of distortion of the local environment around the Eu^{3+} ion in the lattice. According to the Judd-Ofelt theory, a higher asymmetry ratio imply stronger covalence of the Eu−O bonds [32]. The variation of the asymmetry ratio with a variation in Eu^{3+} content is shown in Fig. 12. These results show that the maximum asymmetry ratios were 2.45, 2.63 and 2.52 for the 0.6 mol% $Bi_2O_3:Eu^{3+}$ product at excitation wavelengths at 466, 528 and 534 nm, respectively. This implies that the covalency of the Eu−O bond increased for the 0.6 mol% of Eu^{3+}. A further increase of the dopant content led to the decrease in the crystal asymmetry ratio due to a

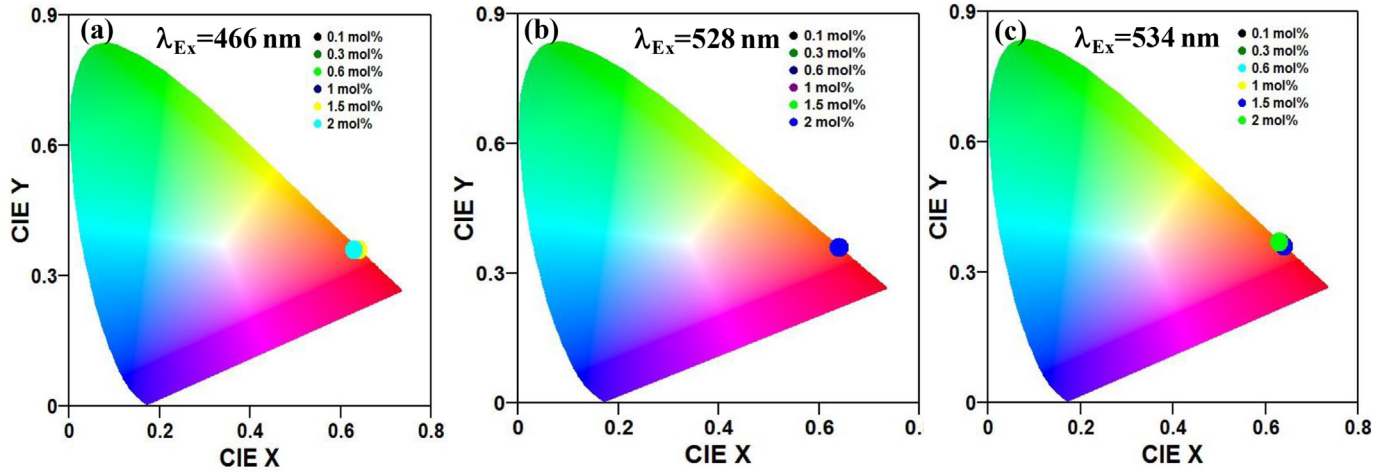

Fig. 14. The CIE diagram of $Bi_2O_3:Eu^{3+}$ for different Eu^{3+} contents with excitation at 466 nm (a), 528 nm (b) and 534 nm (c).

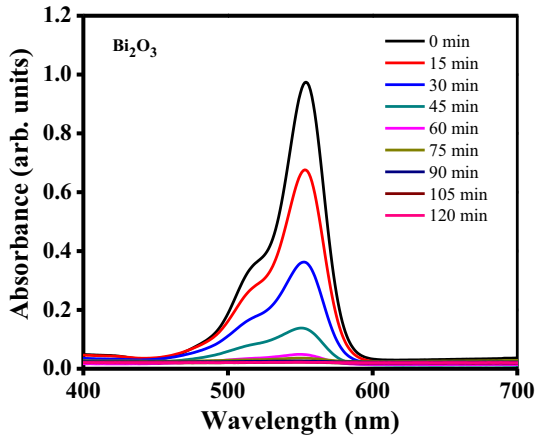

Fig. 15(a). Absorbance spectra of RhB dye in the presence of the Bi_2O_3 under UV–Vis light illumination.

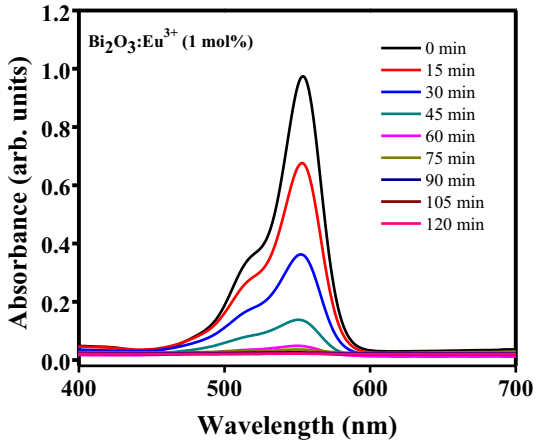

Fig. 15(c). Absorbance spectra of RhB dye in the presence of the $Bi_2O_3:Eu^{3+}$ (1 mol%) under UV–Vis light illumination.

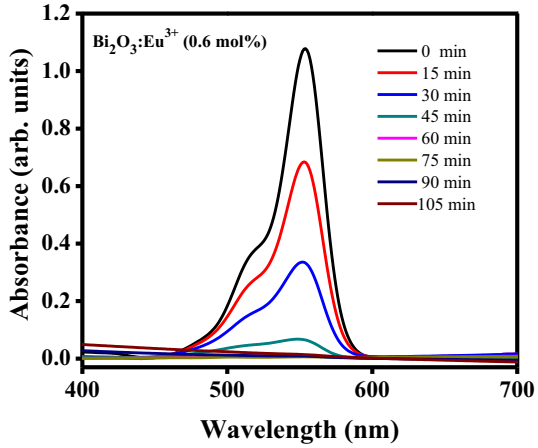

Fig. 15(b). Absorbance spectra of RhB dye in the presence of the $Bi_2O_3:Eu^{3+}$ (0.6 mol%) under UV–Vis light illumination.

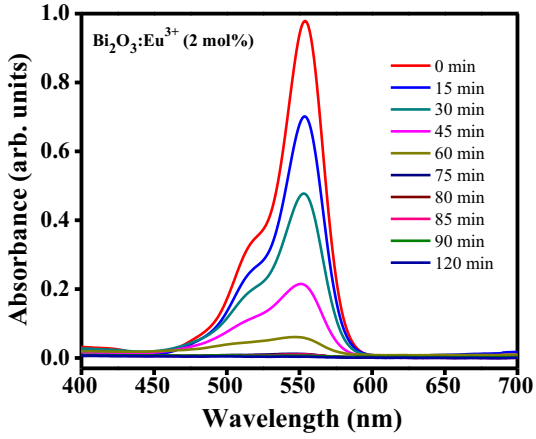

Fig. 15(d). . Absorbance spectra of RhB dye in the presence of the $Bi_2O_3:Eu^{3+}$ (2 mol%) under UV–Vis light illumination.

decrease in the crystallite size. Wang et al. [33] reported the asymmetric ratios of $Y_2O_3:Eu^{3+}$ with various crystallite sizes. His results showed that the asymmetric ratio increased slightly with increasing crystallite size, which confirmed the decrease in local symmetry and hence an increase in red emission. Similar results were observed in the present work. Z. H Shah et al., [21] also reported that a higher chromium content in α-Fe_2O_3, which increased the dislocation density of the product and a decrease in the crystallite size was attributed to the dopant atoms that accumulated at the grain boundaries, preventing the growth in the crystallite size. A similar decrease was observed in the present work. At low dopant content, the Eu^{3+} ions diffused into the Bi_2O_3 lattice. After the optimum concentration of the Eu^{3+} ions was

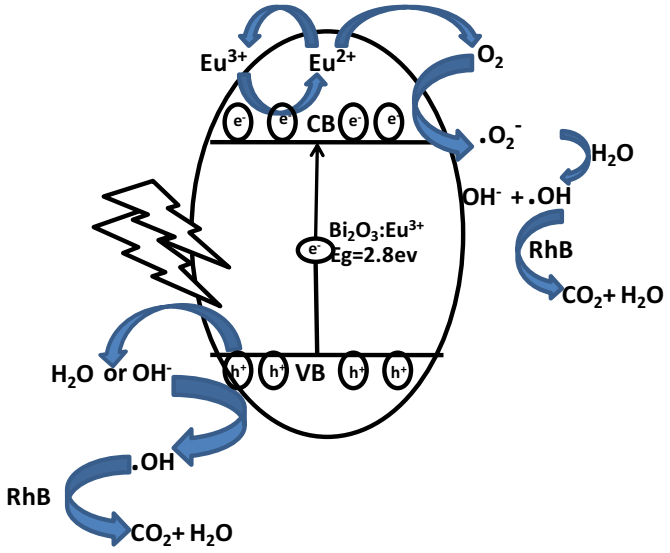

Fig. 16. The photocatalytic degradation mechanism of RhB dye.

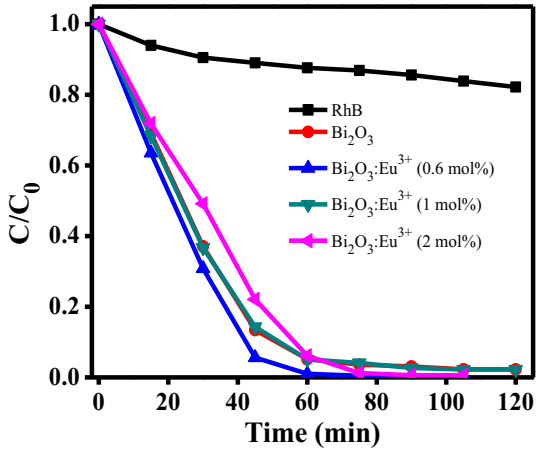

Fig. 17. RhB degradation under UV–Vis radiation of undoped, $Bi_2O_3:Eu^{3+}$ and without photocatalyst.

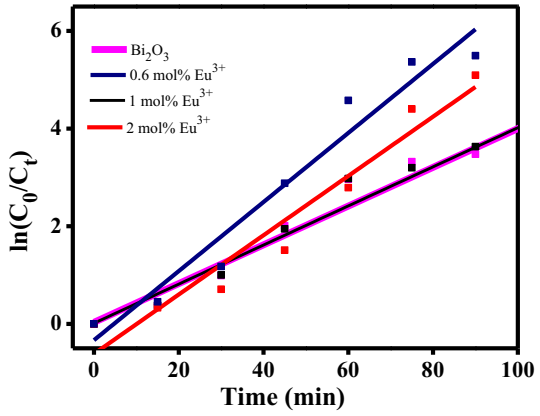

Fig. 18. Semi-logarithmic plots for the photodegradation of RhB in the presence of undoped and $Bi_2O_3:Eu^{3+}$ nanocrystals.

reached, the rest of the Eu^{3+} maybe occupying positions at the grain boundaries [21], resulting in the increase of the cross-relaxation processes in the Eu^{3+} excitation levels and hence a decrease in red emission.

3.7. Time resolved photoluminescence

The PL decay times of the $Bi_2O_3:Eu^{3+}$ nanocrystals were obtained as a function of Eu^{3+} content. Fig. 13 shows the decay curves of the emission at 612 nm excited at 466 nm of the $Bi_2O_3:Eu^{3+}$. The decay time curves for the $Bi_2O_3:Eu^{3+}$ were fitted with a double-exponential function as shown in the inset of Fig. 13 [34]. The obtained fast decay times (τ_1) showed a systematic change from 5.74 to 8.19 μs and the slow decay time (τ_2) component has varied from 226.7 μs to 409.2 μs for the Eu^{3+} content of 0.1 to 2.0 mol%, respectively and are tabulated in Table 3.

In the current study the fastest decay time was measured as 8.19 μs and the slowest decay time was 409.2 μs for the 1.5 mol% and 0.1 mol% Eu^{3+} doping content, respectively. A possible explanation is that the increasing doping content may increase the number of ions occupying the surface states in the nanoscale dimensional materials and these states may be leading to content quenching performance [34,35]. In the current study, the decay time decreased after 1.5 mol% and 0.1 mol% Eu^{3+} doping for the fast and slow decay times, respectively, which supports the emission and excitation spectral analysis reported earlier. In particularly, the strong emission is useful for optoelectronic applications such as display and solid state lighting. A possible explanation for the two different decay rates observed in this study is that the fast decay time curve can be attributed to the presence of non-radiative processes that could be associated to structural imperfection or residual contaminants such as OH^- and CO_2 and maybe the formation of clustering ions, while the slow decay is the result of the direct relaxation of the excited ions.

3.8. Photometric characterization

The International Commission on Illumination (CIE) chromaticity diagrams of $Bi_2O_3:Eu^{3+}$ for different Eu^{3+} contents with excitation at 466 nm, 528 nm and 534 nm are presented in Fig. 14(a–c). The different CIE parameters such as colour coordinates (x,y) (using the GoCIE software) and colour correlated temperature (CCT) (using the McCamy empirical formula [36,37]) were calculated in order to characterize the colour emission for the current Bi/Eu system.;

$$CCT = -437n^3 + 3601n^2 - 6861n + 5514.31$$

where, $n = (x - x_e)/(y - y_e)$ is the inverse of the slope line, and the chromaticity epicentre is at $x_e = 0.3320$ and $y_e = 0.1858$ [36,37].

The calculated colour coordinates indicates that the x and y colour coordinates values were stable (0.64, 0.36) with an increase in the Eu^{3+} content, and are very close to the commercial available $Y_2O_3S:Eu^{3+}$ (0.667, 0.326) red phosphor. Also important is that these values are almost constant for all different excitations investigated in this study. The CCT values of the $Bi_2O_3:Eu^{3+}$ were found to vary from 1989 to 2225 K, which are substantially lower than the normal 5000 K, which is associated with the warm white light used in home appliances.

3.9. Photodegradation of RhB

As control, the UV–Vis spectra variation as a function of time for the RhB dye in the presence of undoped Bi_2O_3 was performed and the results are given in Fig. 15(a). This results clearly indicate a steady decrease in absorption maximum at 554 nm with increasing irradiation time, indicating the relative slow degradation of RhB in the presence of the undoped- photocatalyst. The same reaction was monitored in the presence of Eu-doped Bi_2O_3 to determine the influence, if any of the new products. The results obtained from this comparative study indicate that the photocatalytic activity of the $Bi_2O_3:Eu^{3+}$ (doped) was higher than that of the undoped Bi_2O_3 as shown in Figs. 15(b)–15(d). The higher photocatalytic activity of the $Bi_2O_3:Eu^{3+}$ compared to undoped Bi_2O_3 is attributed to the presence of the Eu ions, which improves the catalytic degradation of the RhB dye. The 4f electrons

Table 4
Parameters of photocatalytic degradation of the RhB solutions by undoped and Bi_2O_3:Eu^{3+}.

Samples	Rate constants, k	Correlation constants, R^2	Photodegradation efficiency, η (%)
Bi_2O_3	0.0397 ± 0.0036	0.94	97.7
Bi_2O_3:Eu^{3+} (0.6 mol%)	0.0710 ± 0.0067	0.95	99.7
Bi_2O_3:Eu^{3+} (1.0 mol%)	0.0400 ± 0.0033	0.96	97.7
Bi_2O_3:Eu^{3+} (2.0 mol%)	0.0607 ± 0.0065	0.94	99.3

transitions within the rare earths are known to lead to the optical adsorption of the catalyst enforcement [38].

The Eu^{3+} cations are well-known to be good electron acceptors, which can capture excited electrons and can facilitate in the separation of photogenerated electron–hole pairs, which can promote charge transfer from the surface of the photocatalyst to the substrate [38]. A possible mechanism explaining the photocatalytic behavior of doped Bi_2O_3 is presented in Eqs. (1)–(10). Incident UV–Vis light strikes the surface of the α-Bi_2O_3:Eu^{3+} nanocrystals, and generates electron holes in the valence band (VB) and electrons in the conduction band (CB) (Eq. (1)) are produced. After separation and transfer of the photogenerated charge carriers, a redox reaction takes place between the adsorbate and charge carriers on the surface of the Bi_2O_3 host. The holes generated in the VB reacted with water (H_2O) to form OH radicals and hydrogen cations (H^+) (Eq. (2)) or alternatively the holes in the VB react with the hydroxyl anions (OH^-) to form hydroxyl radicals (OH) (Eq. (3)). The electrons produced in the CB reacts with the trivalent europium cation (Eu^{3+}) to generate divalent europium (Eu^{2+}) (Eq. (4)). This newly formed Eu^{2+} ion reacts with atmospheric O_2, re-generating Eu^{3+} as well as a superoxide anion radical (O_2^{-}) (Eq. (5)), which can react with the earlier produced H^+ (Eq. (2))·to forma water radical species HO_2· (Eq. (6)). In the next step, the HO_2 radical accepts an electron to produce HO_2^- (Eq. (7)), which can react with surface H^+ to produce hydrogen peroxide (H_2O_2) (Eq. (8)). In the penultimate step the H_2O_2 accepts an electron to produce OH^- and a hydroxyl radical OH· (Eq. (9)). The newly formed OH· is an excellent oxidizing agent (STD reduction potential = +2.8 V), which have the ability to oxidize the RhB dye in an aqueous solution to produce CO_2 and H_2O as products (Eq. (10)) [10,39]. The photocatalytic degradation mechanism is also illustrated in Fig. 16. These results clearly indicate that the photocatalytic activity of the Bi_2O_3 can be enhanced by its doping with Eu^{3+} (0.6 mol %) as confirmed by the red shift in the optical adsorption edge of Bi_2O_3. The results further suggest that an optimum concentration of Eu^{3+} ions in the Bi_2O_3 product was attained to effectively separate the photogenerated holes and electrons. It is anticipated that at higher Eu^{3+} ion content (≥1 mol%), the space charge region becomes very narrow, which prevent or limit the penetration depth of light into the catalyst, which exceeds the space charge layer. This result in the easy recombination of the electron-hole pairs, which lead to a decrease in the photocatalytic activities of the doped Bi_2O_3 samples [25]. The photocatalytic activity for 2 mol% Bi_2O_3:Eu^{3+} samples showed a slight increase, but comparatively less than the 0.6 mol% Eu^{3+} as shown in Fig. 17, which might be due to the mixed phase of α- and β-Bi_2O_3 obtained at these Eu^{3+} content.

$$\alpha - Bi_2O_3 \rightarrow e^- \text{ (CB)} + h^+ \text{ (VB)} \quad (1)$$

Oxidation at VB

$$h^+ + H_2O \rightarrow \cdot OH + H^+ \quad (2)$$

$$h^+ + OH^- \rightarrow \cdot OH \quad (3)$$

Reduction at CB

$$Eu^{3+} + e^- \rightarrow Eu^{2+} \quad (4)$$

$$Eu^{2+} + O_2 \rightarrow Eu^{3+} + \cdot O_2^- \quad (5)$$

$$\cdot O_2^- + H^+ \rightarrow \cdot HO_2 \quad (6)$$

$$\cdot HO_2^- + e^- \rightarrow HO_2^- \quad (7)$$

$$HO_2^- + H^+ \rightarrow H_2O_2 \quad (8)$$

$$H_2O_2 + e^- \rightarrow OH^- + \cdot OH \quad (9)$$

$$OH^-/\cdot OH + RhB \rightarrow CO_2^- + H_2O \quad (10)$$

The catalytic activity of undoped and Bi_2O_3:Eu^{3+} were kinetically evaluated by determining the 1st order rate constants by assuming pseudo- first-order conditions as indicated in Eq. (11) [11].

$$\ln(C_0/C) = kt \quad (11)$$

where C_0 and C are the concentration of RhB in the aqueous solution at time 0 and t, respectively and k is the pseudo first-order rate constant. Graphs representing plots of $\ln(C_0/C)$ as a function of irradiation time (t) are shown in Fig. 18. The goodness of fitting is represented by (R^2) of the plot. The regression correlation coefficient obtained for the different reactions were calculated as 0.94, 0.95, 0.96 and 0.94 for the undoped, 0.6 mol%, 1 mol% and 2 mol% of Bi_2O_3:Eu^{3+}, respectively. The calculated pseudo-first order rate constants tabulated in Table 4 indicate that the maximum rate constant value (quickest) was observed for the 0.6 mol% doped Bi_2O_3:Eu^{3+} sample and is attributed to the higher surface area of the Bi_2O_3 particles. The photodegradation efficiency (η) of the undoped, 0.6, 1.0 and 2.0 mol% of Bi_2O_3:Eu^{3+} were calculated with the expression given by [40];

$$\eta\,(\%) = \frac{C_0 - C}{C_0} \times 100$$

where C_0 is the concentration of RhB before irradiation ($t = 0$) and C is the concentration of RhB after a certain irradiation time (t). The calculated values are tabulated in Table 4. Degradation efficiency of 97% plus was obtained for the undoped sample, whereas Bi_2O_3:Eu^{3+} (0.6 mol%) sample showed 99% plus degradation efficiency.

4. Conclusion

The undoped and Bi_2O_3:Eu^{3+} doped nanocrystals were prepared by the citrate sol-gel method and PEG which was successfully used as a surfactant to control the particle sizes.SEM images of the final products confirmed the PEG covering of the surfaces of both undoped and Bi_2O_3:Eu^{3+} nanoparticles. The optical reflectance revealed that, the bandgap has decreased after the incorporation of the Eu^{3+} ions into the Bi_2O_3 nanocrystal. XPS results of the Bi_2O_3:Eu^{3+} confirmed the Eu^{3+} ions replaced some of the Bi^{3+} sites in the newly produced Bi_2O_3 crystal. Excitations at 466, 528 and 534 nm showed that the relative intensity of the electric dipole to maganetic dipole emission increased with an increase in the Eu^{3+} content from 0.1 to 0.6 mol% and resulting in an increase in the crystallite size and a decrease in the dislocation density. A further increase of the Eu^{3+} content led to a decrease in the PL intensity due to the increase of the dislocation density confirming that the Eu^{3+} ions were in a strong crystal field environment. The Bi_2O_3:Eu^{3+} (0.6 mol%) exhibited a higher photocatalytic activity than that of undoped Bi_2O_3. The enhanced photocatalytic activity was attributed to an increase in the surface area of the Bi_2O_3 nanoparticles. These results confirmed that the Eu^{3+} cations in the crystal structure improve the electron acceptor ability and facilitate the reduction recombination of photoinduced electron-hole pairs in the crystal structure

and improve the absorption and utilization ability to UV–Vis radiation. These nanophosphors proved to be good candidates for red light emission, which effectively photocatalyst RhB dye degradation under UV–Vis radiation.

Acknowledgments

The authors express their sincere thanks to the South African Research Chairs Initiative of the Department of Science and Technology and the National Research Foundation of South Africa (84415). The financial assistance from the University of the Free State, South Africa is highly recognized.

References

[1] H. Oudghiri-Hassania, S. Rakass, F.T. Al Wadaani, K.J. Al-ghamdi, A. Omer, M. Messali, M. Abboudi, Synthesis, characterization and photocatalytic activity of α-Bi_2O_3 nanoparticles, Journal of Taibah University for Science 9 (4) (2015) 508–512.
[2] M.G. Ma, J.F. Zhu, R.C. Sun, Y.J. Zhu, Microwave-assisted synthesis of hierarchical Bi_2O_3 spheres assembled from nanosheets with pore structure, Mater. Lett. 64 (2010) 1524–1527.
[3] S. Singh, R. Sharma, Bi_2O_3/Ni-Bi_2O_3 system obtained via Ni-doping for enhanced PEC and photocatalytic activity supported by DFT and experimental study, Sol. Energy Mater. Sol. Cells 186 (2018) 208–216.
[4] S. Selvarajan, A. Suganthi, M. Rajarajan, K. Arunprasath, Highly efficient $BiVO_4$/WO_3 nanocomposite towards superior photocatalytic performance, Powder Technol. 307 (2017) 203–212.
[5] S. Selvarajan, A. Suganthi, M. Rajarajan, M.M. Shrividhya, Fabrication of highly efficient mesoporous $NaBiO_3$/ZnO nanocomposites for recyclable photocatalytic degradation of organic pollutants, Opt. - Int. J. Light Electron Opt. 153 (2018) 16–30.
[6] V. Ramasamy Raja, A. Karthika, A. Suganthi, M. Rajarajan, Facile synthesis of $MnWO_4$/BiOI nanocomposites and their efficient photocatalytic and photoelectrochemical activities under the visible light irradiation, Journal of Science: Advanced Materials and Devices 3 (2018) 331–341.
[7] A. Prakash, M. Dan, S. Yu, S. Wei, Y. Li, F. Wang, Y. Zhou, In_2S_3/CuS nanosheet composite: an excellent visible light photocatalyst for H_2 production from H_2S, Sol. Energy Mater. Sol. Cells 180 (2018) 205–212.
[8] M.Z. Ghori, S. Veziroglu, B. Henkel, A. Vahl, O. Polonskyi, T. Strunskus, F. Faupel, O.C. Aktas, A comparative study of photocatalysis on highly active columnar TiO_2 nanostructures in air and in-solution, Sol. Energy Mater. Sol. Cells 178 (2018) 170–178.
[9] D.P. Dutta, M. Roy, A.K. Tyagi, Dual function of rare earth doped nano Bi_2O_3: white light emission and photocatalytic properties, Dalton Trans. 41 (2012) 10238–10248.
[10] S. Sood, S.K. Umarb, Mehta, S.K. Kansal, α-Bi_2O_3 nanorods: an efficient sunlight active photocatalyst for degradation of rhodamine B and 2,4,6-trichlorophenol, Ceram. Int. 41 ((2015) 3355–3364.
[11] Y. Yan, Z. Zhou, Y. Cheng, L. Qiu, C. Gao, J. Zhou, Template-free fabrication of α- and β-Bi_2O_3 hollow spheres and their visible light photocatalytic activity for water purification, J. Alloy. Compd. 605 (2014) 102–108.
[12] T.S. Chan, C.C. Kang, R.S. Liu, L. Chen, X.N. Liu, J.J. Ding, J. Bao, C. Gao, Combinatorial study of the optimization of Y_2O_3: Bi, Eu red phosphors, J. Comb. Chem. 9 (3) (2007) 343–346.
[13] S. Ashwini, S.C. Prashantha, R. Naik, H. Nagabhushana, Enhancement of luminescence intensity and spectroscopic analysis of Eu^{3+} activated and Li^+ charge-compensated Bi_2O_3 nanophosphors for solid-state lighting, J. Rare Earths 37 (2019) 356–364.
[14] H. Weidong, Q. Wei, W. Xiaohong, D. Xianbo, C. Long, J. Zhaohua, The photocatalytic properties of bismuth oxide films prepared through the sol–gel method, Thin Solid Films 515 (2007) 5362–5365.
[15] E.J. Rivera, L.A. Tran, M. Hernandez-Rivera, ´.D. Yoon, A.G. Mikos, I.A. Rusakova, B.Y. Cheong, M. da Graça Cabreira-Hansen, J.T. Willerson, E.C. Perin, L.J. Wilson, Bismuth @ US-tubes as a potential contrast agent for X-ray imaging applications, J. Mater. Chem. B 1 (2013) 4792–4800.
[16] D. Barreca, F. Morazzoni, G.A. Rizzi, R. Scotti, E. Tondello, Molecular oxygen interaction with a spectroscopic and Bi_2O_3: spectromagnetic investigation, Phys. Chem. Chem. Phys. 3 (2001) 1743–1749.
[17] M.S. Chen, S.H. Chen, F.C. Lai, C.Y. Chen, M.Y. Hsieh, W.J. Chang, J.C. Yang, C.K. Lin, Sintering temperature-dependence on radiopacity of $Bi_{(2-x)}$ $Zr_xO_{(3+x/2)}$ powders prepared by sol-gel process, Materials 11 (1685) (2018) 1–14.
[18] L.G. Sillen, Z. Krist. Krist. Krist. Krist. 103 (1941) 274.
[19] L.G. Sillen, Ark. Kemi, The crystal structure of monoclinic Bi_2O_3, Mineral. Geol. 12 (1938) 1.
[20] G. Malmros, The crystal structure of α-Bi_2O_3, Acta Chem. Scand. 24 (1970) 384–396.
[21] Z.H. Shah, S. Riaz, Z.N. Kayani, S. Naseem, Size Distribution and Magnetic Optimization of Phase Pure Chromium Doped Magnetite Nanoparticles, the 2016 World Congress on Advances in Civil, Environmental and Material Research (ACEM16), Jeju Island, Korea, August 28-Spetmber 1, (2016).
[22] B.D. Cullity, Elements of X-Ray Diffraction, Addison Wesley Publishing Company, USA, 1956.
[23] Y. Sahai, V. Kumar, N. Agarwal, Goswami, Doping concentration driven morphological evolution of Fe doped ZnO nanostructures, J. Phys. D. Appl. Phys. 116 (2014) 164315 (12 pages).
[24] Y. Shi, L. Luo, Y. Zhang, Y. Chen, S. Wang, Lingxin Li, Y. Long, F. Jiang, Synthesis and characterization of α/β-Bi_2O_3 with enhanced photocatalytic activity for 17α-ethynylestradiol, Ceram. Int. 43 (2017) 7627–7635.
[25] S. Wu, J. Fang, X. Xu, Z. Liu, X. Zhu, W. Xu, Microemulsion synthesis, characterization of highly visible light responsive rare earth-doped Bi_2O_3, Photochem. Photobiol. 88 (2012) 1205–1210.
[26] Y. Zhang, B. Fluegel, M.C. Hanna, A. Mascarenhas, L.W. Wang, Y.J. Wang, X. Wei, Impurity perturbation to the host band structure and recoil of the impurity state, Phys. Rev. B 68 (2003) 075210 (4pages).
[27] J.F. Moulder, W.F. Strickle, P.E. Sobol, K.D. Bomben, Handbook of X-ray Photoelectron Spectroscopy, ULVAC-PHI Inc, 1992.
[28] Y. Huang, J. Qin, C. Hu, X. Liu, D. Wei, H.J. Seo, Cs-doped α-Bi_2O_3 microplates: hydrothermal synthesis and improved photochemical activities, Appl. Surf. Sci. 473 (2019) 401–408.
[29] V. Kumar, H.C. Swart, O.M. Ntwaeaborwa, R.E. Kroon, J.J. Terblans, S.K.K. Shaat, A. Yousif, M.M. Duvenhage, Origin of the red emission in zinc oxide nanophosphors, Mater. Lett. 101 (2013) 57–60.
[30] T. Liu, W. Xu, X. Bai, H. Song, Tunable silica shell and its modification on photoluminescent properties of Y_2O_3:Eu^{3+}@SiO_2 nanocomposites, J. Appl. Phys. 111 (064312) (2012) (8 pages).
[31] P. Packiyaraj, P. Thangadurai, Structural and photoluminescence studies of Eu^{3+} doped cubic Y_2O_3 nanophosphors, J. Lumin. 145 (2014) 997–1003.
[32] J.W. Wang, H.W. Song, X.G. Kong, H.S. Peng, B.J. Sun, B.J. Chen, J.H. Zhang, W. Xu, Fluorescence properties of trivalent europium doped in various niobate codoped glasses, J. Appl. Phys. 93 (3) (2003) 1482–1486.
[33] W.N. Wang, W. Widiyastuti, T. Ogi, I.W. Lenggoro, K. Okuyama, Correlations between crystallite/particle size and photoluminescence properties of submicrometer phosphors, Chem. Mater. 19 (2007) 1723–1730.
[34] K.B. Eisenthal, S. Siegel, Influence of resonance transfer on luminescence decay, J. Chem. Phys. 41 (1964) 652–655.
[35] M. Inokuti, F. Hirayama, Influence of energy transfer by the exchange mechanism on donor luminescence, J. Chem. Phys. 43 (1965) 1978–1989.
[36] L.L. Noto, O.M. Ntwaeaborwa, M.Y.A. Yagoub, H.C. Swart, Improvement of the photoluminescent intensity of $ZnTa_2O_6$:Pr^{3+} phosphor, Mat. Res. Bull. 55 (2014) 150–155.
[37] N.J. Shivaramu, K.R. Nagabhushana, B.N. Lakshminarasappa, Fouran Singh, Ion beam induced luminescence studies of solgel derived Y_2O_3:Dy^{3+} nanophosphors, J. Lumin. 169 (2016) 627–634.
[38] M. Wang, Y. Che, C. Niu, M. Dang, D. Dong, Effective visible light-active boron and europium co-doped $BiVO_4$ synthesized by sol–gel method for photodegradation of methyl orange, J. Hazard. Mater. 262 (2013) 447–455.
[39] Y. Zhang, G. Zhu, J. Gao, R. Zhu, M. Hojamberdiev, C. Wang, P. Liu, Superior-performance spherical-like Eu-doped Bi_5O_7I photocatalysts for the removal of organic pollutants under visible light irradiation, J. Mater. Sci. Mater. Electron. 28 (2017) 11034–11045.
[40] P. Malathy, K. Vignesh, M. Rajarajan, A. Suganthi, Enhanced photocatalytic performance of transition metal doped Bi_2O_3 nanoparticles under visible light irradiation, Ceram. Int. 40 (2014) 101–107.